NANO LETTERS

pubs.acs.org/NanoLett Letter

Nanoscale Localized Phonons at Al_2O_3 Grain Boundaries

Jingyuan Yan, Ruochen Shi, Jiake Wei, Yuehui Li, Ruishi Qi, Mei Wu, Xiaomei Li, Bin Feng,* Peng Gao,* Naoya Shibata, and Yuichi Ikuhara*

Cite This: https://doi.org/10.1021/acs.nanolett.3c04149 Read Online

ACCESS | Metrics & More | Article Recommendations | Supporting Information

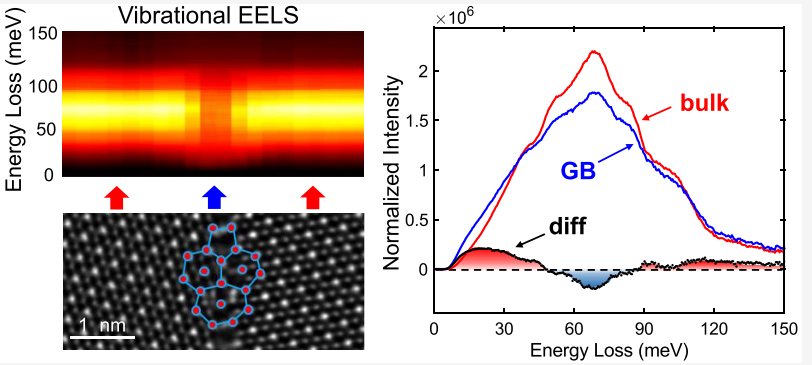

ABSTRACT: Nanoscale defects like grain boundaries (GBs) would introduce local phonon modes and affect the bulk materials' thermal, electrical, optical, and mechanical properties. It is highly desirable to correlate the phonon modes and atomic arrangements for individual defects to precisely understand the structure−property relation. Here we investigated the localized phonon modes of Al_2O_3 GBs by combination of the vibrational electron energy loss spectroscopy (EELS) in scanning transmission electron microscope and density functional perturbation theory (DFPT). The differences between GB and bulk obtained from the vibrational EELS show that the GB exhibited more active vibration at the energy range of <50 meV and >80 meV, and further DFPT results proved the wide distribution of bond lengths at GB are the main factor for the emergence of local phonon modes. This research provides insights into the phonon-defect relation and would be of importance in the design and application of polycrystalline materials.

KEYWORDS: *electron energy loss spectroscopy, localized phonon, vibration mode, grain boundary, density functional perturbation theory, Al_2O_3*

The lattice vibration behavior of the crystal material, namely, the phonon modes, is an important material characteristic and related with many material properties like thermal conductivity, thermoelectric performance, electrical transportation, and structural stability.[1−5] In practical materials, there usually exist defects such as grain boundaries (GBs) and dislocations, which have different atomic structures and chemical bond environments, that are expected to exhibit localized but different phonon modes[6−8] due to the unique force constants. The differences between the "local defect" and "global bulk" phonon structure would result in phonon scattering during the phonon transport, and therefore affect the materials' overall properties.[9−11] For example, the thermal conductivity of a polycrystalline could be expressed as $\lambda_{poly}^{-1} = \frac{1}{\lambda_{crystal}} + nR_{int}^{*}$, where $\lambda_{crystal}$ is the thermal conductivity of the single crystal, R_{int}^{*} is the thermal resistance of a GB, and n is the number of GBs crossed by the heat flow in unit area.[12] Macroscopic measurements show an inverse relation between the thermal conductivity values versus the density of GBs in ceramics like Al_2O_3 and MgO. Specifically, the existence of each GB in Al_2O_3 would introduce an extra resistance of thermal transportation of $\sim 0.9 \times 10^{-8}$ m^2 KW^{-1} on average.[12] However, the phonon modes of these GBs and the correlation between local phonons and atomic structures remain largely unclear due to challenges in the simultaneous measurement of local phonons and atomic structure.

For bulk materials, the phonons can be measured using infrared-Raman (IR) spectroscopy, high-resolution electron energy loss spectroscopy (HREELS), inelastic neutron scattering (INS), inelastic X-ray scattering (IXS), scanning near-field optical microscopy (SNOM), *etc.* However, the

Received: October 29, 2023
Revised: March 4, 2024
Accepted: March 6, 2024

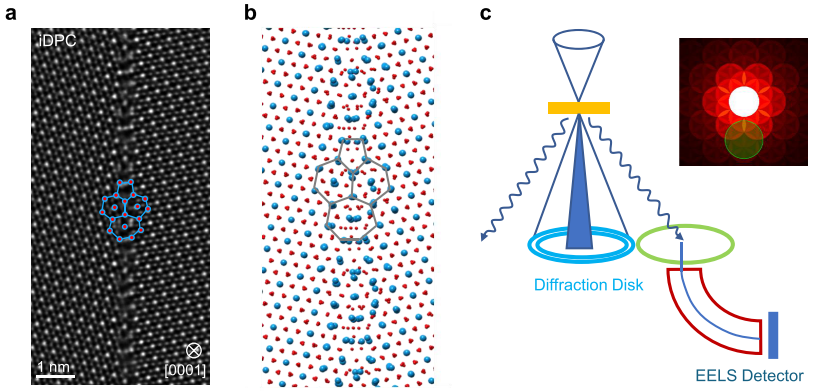

Figure 1. The atomic structure of Al_2O_3GB and EELS measurement setup. (a) An iDPC image of the [0001] oriented ∑7a Al_2O_3 GB; (b) the [0001] direction projection of the simulated GB; (c) the schematic diagram of the off-axis EELS measurement. The top right inset shows the simulated electron diffraction pattern where the green circle highlights the EELS collection angle.

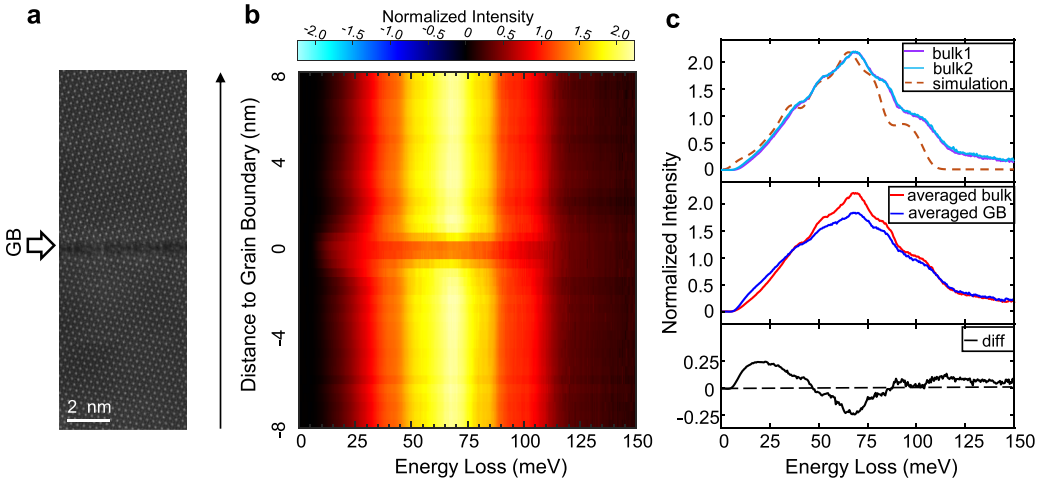

Figure 2. Experimental result of the phonon measurement. (a) HAADF image of the area for EELS measurement; (b) intensity mapping of measured phonon spectra across the GB; (c) comparison of the phonon spectra of the GB and bulk area.

limited spatial resolution of these methods makes it challenging to probe the nanoscale defects like dislocation and GBs, not to mention simultaneously correlating with the local atomic arrangement.[13−17] Recent advances in monochromated EELS and aberration-corrected STEM enable phonon measurement (namely, vibrational EELS spectrum measurement) for nanoscale defects, atomic-scale heterointerfaces, or even single point defects.[18−30] Here, we used STEM-EELS to study the local phonons of Al_2O_3 GBs. Al_2O_3 exhibits high thermal conductivity, chemical stability, and mechanical strength and, thus, is widely used as heat dissipation materials and light windows in the fields of semiconductor and optical devices.[31−33] Such properties in the Al_2O_3 ceramics would be largely affected due to the existence of GB through the local phonon interactions, while the knowledge of such localized phonon structures is still lacking.[34]

In this study, the atomic structure-phonon relations of Al_2O_3 GBs were revealed by a combination of atomic-scale vibrational EELS measurement and density functional perturbation theory (DFPT) calculation. We find that the GBs exhibit quite different vibrational spectra compared to that of the bulk at a space range of around 1.5 nm. The GB shows more active vibration at the energy range of <50 meV and >80 meV and lower intensity at the energy range of 50−80 meV. DFPT results indicate the wider distribution of bond lengths at GB mainly accounts for emergence of the local vibrational modes. Besides, such a tendency is also found in other types of GBs with different atomic structures, while local phonon modes are less sensitive to the GB structures. These findings provide new insights into understanding the GB properties that are closely related with phonon processes, such as heat transportation, and would be of great importance in guiding the material design and fabrication processes via the GB engineering.

Figure 1a shows an integrated differential phase contrast (iDPC) image of a Σ7a GB observed from the [0001] direction. The bright spots correspond to the Al and O atom columns while O shows relative lower intensity due to its smaller atomic number.[35] The structure unit of the GB core can be described as the combination of a 5-ring, two 6-rings, and a 7-ring, which is consistent with previous experimental observations.[36−38] Figure 1b shows the most stable GB structure relaxed by molecular dynamic simulation reported from a previous study.[39] The experimentally observed structure in Figure 1a is in excellent agreement with the calculations in Figure 1b.

To extract the GB phonon modes, an off-axis EELS geometry with large convergence semiangle was set to obtain the spectra comparable to the phonon DOS,[40] as shown in

https://doi.org/10.1021/acs.nanolett.3c04149
Nano Lett. XXXX, XXX, XXX−XXX

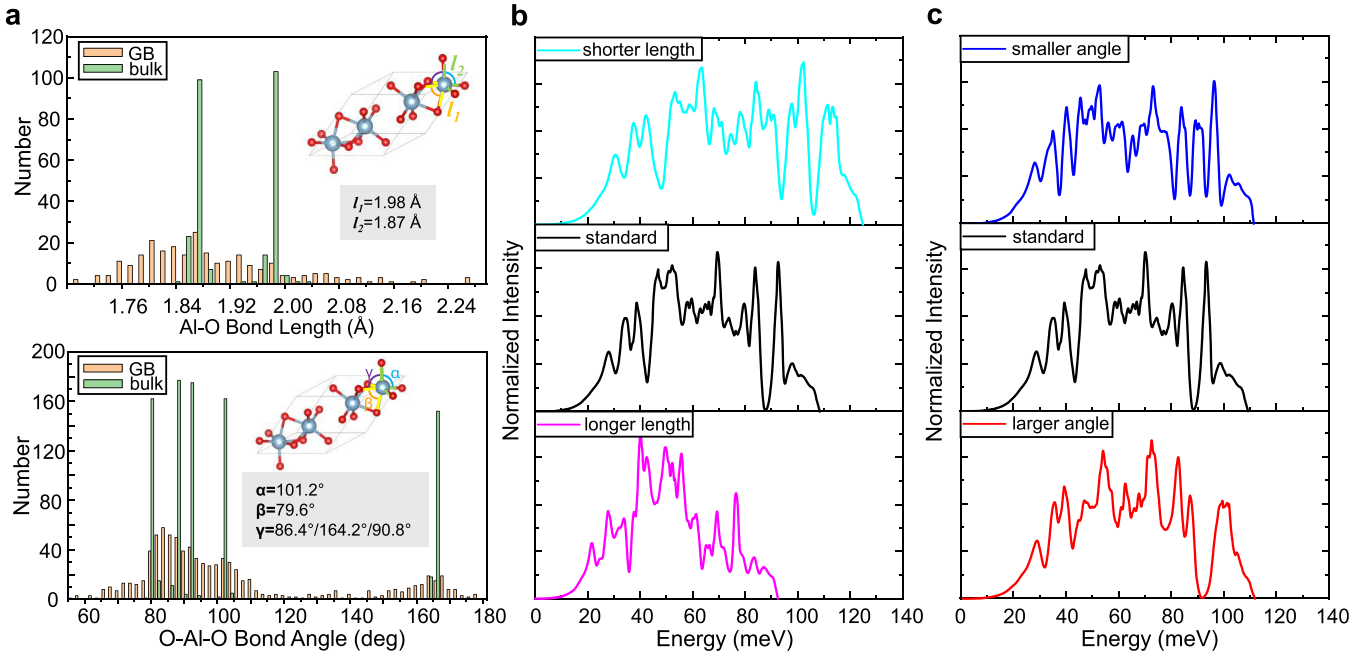

Figure 3. The analysis of the bond length and angle of the GB and their effects on the GB phonon. (a) The distribution of the bond length and bond angle of the GB and bulk area, with values of the standard Al_2O_3 unit cell marked in insets; (b) the phonon DOS of cells with different bond lengths; (c) the phonon DOS of cells with different bond angles.

Figure 1c. The details are given in the Methods. Figure 2a shows a high-angle annular dark-field (HAADF) image of the GB, and the corresponding line profile mapping of the background-subtracted vibrational EELS spectra across the GB is shown in Figure 2b. The phonon signals change abruptly near the GB within approximately 1.5 nm, indicating the high localization nature, which exhibits similar width of transition area reported in the diamond-cBN heterointerface[41] and is slightly narrower than that of the staking fault in SiC.[42] To quantitatively compare the two spectra of GB and bulk, the difference was further calculated as diff = $\text{spectrum}_{\text{bulk}} - \text{spectrum}_{\text{GB}}$ and shown in Figure 2c. The main feature is that at energy range of <50 meV and >80 meV, a positive diff value is obtained, indicating more active vibration in the GB area than that of the bulk, while at energy range of 50−80 meV, the diff value is calculated to be below 0, indicating a rather smaller phonon population in this energy range and, thus, vibration with lower activities at the GB region.

To understand the origin of the phonon DOS change in GB, DFPT calculations were carried out. Although a full calculation of GB phonon DOS is not realistic due to the huge cost for the complex GB atomic structure, we tried to investigate such phonon DOS change from the structural point of view. It is known that at GBs, the atom positions are greatly shifted to compensate for the difference in orientation of the two grains, which means the change of bond length and bond angle would be the most prominent structural difference at the GBs. Accordingly, we have statistically analyzed the bond lengths and bond angles using the reported GB structure model,[39] as shown in Figure 3a. We analyzed about 300 Al−O bond length values and 900 O−Al−O bond angle values within a 1.5 nm wide area in the bulk and around the GB (this width is determined by the experimentally measured EELS broadening width in Figure 2). In the bulk region, the bond lengths and bond angles show certain fixed values that are determined by the crystallographic features of Al_2O_3. In contrast, the GB exhibits a rather dissipated distribution of both bond lengths and bond angles. Considering the force constants are sensitive to the local bond environments, it is highly possible that these structural feature changes might account for the unique GB phonon DOS.

To analyze the effect of the bond length and bond angle on the localized phonon DOS, Al_2O_3 unit cells with varied bond length and angles were artificially constructed and relaxed, and their phonon DOS were calculated (detailed values of the bond angle and length were given at Table 1). Drastic changes

Table 1. Structure Parameters of the Lattice with Different Bond Angles and Lengths

Notion	O−Al−O bond angle		O−Al−O bond length	
	α (deg)	β (deg)	l_1 (Å)	l_2 (Å)
Standard	101.2	79.6	1.98	1.87
Smaller angle	95.57 (−5%)	75.62(−5%)	1.98	1.87
Larger angle	106.26 (+5%)	83.58 (+5%)	1.98	1.87
Shorter length	101.2	79.6	1.88 (−5%)	1.78 (−5%)
Longer length	101.2	79.6	2.08 (+5%)	1.96 (+5%)

were found with the change of bond length in Figure 3b; i.e., when the bond length is reduced by 5%, the cutoff energy increases to about 124 meV, whereas it decreases to 97 meV when the bond length is increased by 5%. However, with a 5% change in bond angle in Figure 3c, the phonon DOS showed subtle changes in the shape of peaks compared with the standard Al_2O_3, while the overall curve shapes remain almost unchanged and cutoff energies are all still resided in 108−111 meV. Besides, it should be noted that the changes of the curve in Figure 3b are not simple proportional scaling, indicating for the different phonon branches the effects of bond length change could be different. These results show that the phonon structure is much more sensitive to the bond length change than to the bond angle.

https://doi.org/10.1021/acs.nanolett.3c04149
Nano Lett. XXXX, XXX, XXX−XXX

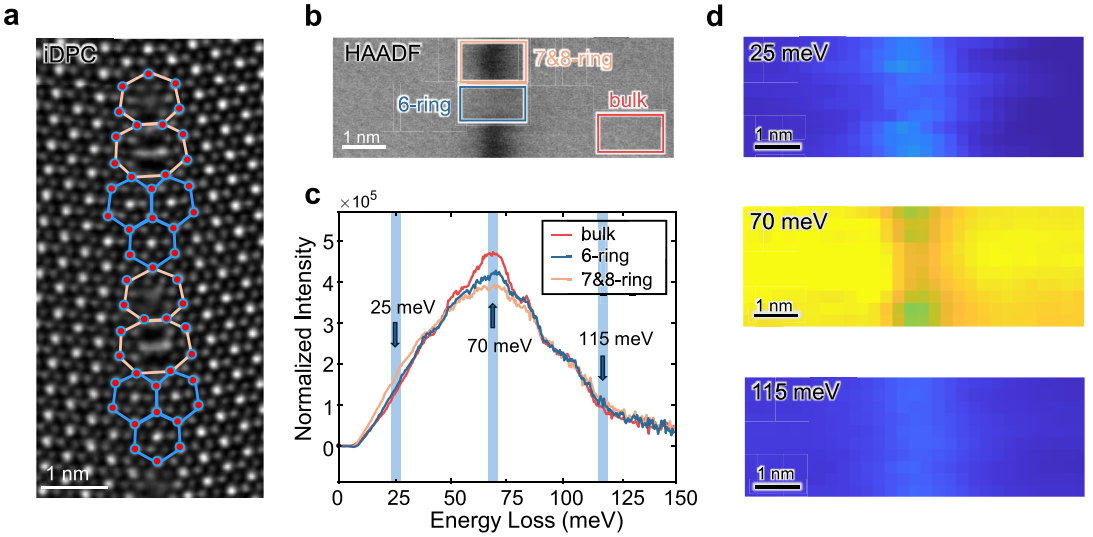

Figure 4. Spatially different EELS response in the ∑19a GB. (a) An iDPC image for the ∑19a GB, with 7&8-ring area and 6-ring area marked with light orange and blue polygons; (b) the HAADF image obtained simultaneously with the EELS spectra; (c) the spectra of the 7&8-ring, 6-ring areas compared with bulk; (d) the two-dimensional mapping of the EELS signals obtained within 5 meV-wide energy windows centered at 25, 70, and 115 meV, which obviously showing different EELS response at the 6-ring and 7&8-ring areas. Brighter color represents higher intensity.

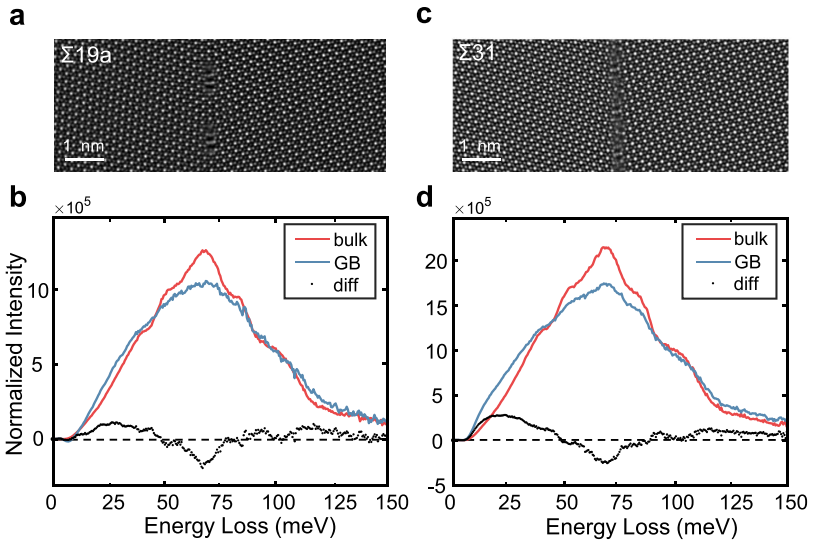

Figure 5. The vibrational spectra of GBs with different tilt angles. (a) An iDPC image of the ∑19a Al_2O_3 GB; (b) the vibrational EELS spectra of the ∑19a Al_2O_3 GB; (c) an iDPC image of the ∑31 Al_2O_3 GB; (d) the vibrational EELS spectra of the ∑31 Al_2O_3 GB.

Such a conclusion is further validated by our vibrational spectra measurements of GBs with different misorientations. Figure 4 shows the spatially different EELS response of the ∑19a GB. As shown in Figure 4a, the ∑19a GB unit consists of a 7-ring, an 8-ring, followed by three 6-rings. The 6-ring area shows rather smaller change in bond length than the 7&8-ring area while the misorientation is basically fitted by changes in bond angles. Figure 4c shows the vibrational spectra of the 6-ring and 7&8-ring areas compared to bulk, of which the measurements were performed at areas denoted in Figure 4b. One can tell that the 7&8-ring area shows much larger change than the 6-ring area, while the 6-ring area exhibits as an intermediate of the 7&8-ring area and bulk. Such a difference is clearly visualized in the EELS mapping in Figure 4d, especially at 25 and 70 meV, where the 7&8-ring areas show much higher and lower intensity, respectively. These results further strengthen our conclusion that the change of local phonon is mainly caused by the changes in bond length.

On the other hand, with different substructures mixed in the GBs, the EELS responses of the integrated GB areas show rather low dependency to the misorientation. As shown in Figure 5, the EELS spectra of ∑19a and ∑31GBs (with misorientation of 14.1°, 18.8°) show similar characters with that of the ∑7a GB (with misorientation of 23.3°): at the GBs higher vibration intensity at energy ranges of <50 meV and >80 meV, and lower vibration intensity at 50−80 meV. This is resulted from their similar bond length distributions in the integrated GB areas (see bond length distribution comparison of ∑7a and ∑31 GB in Figure S1), which results in a similar change in the force constants and such universal phonon DOS change in Al_2O_3 GBs.

Our results show localized phonon DOS of Al_2O_3 GB are not sensitive to the misorientation of the two neighboring

https://doi.org/10.1021/acs.nanolett.3c04149
Nano Lett. XXXX, XXX, XXX−XXX

grains, which is different than the common assumption. Instead, it is mainly determined by GB's intrinsic structural characteristics, i.e., the local bonding situation. By quantitively and respectively introducing changes in bond length and bond angle into the Al_2O_3 unit cell during DFT calculation, we further validated the wide distribution of bond length as the dominating factor in determining the local phonons. However, the wide range distribution of the bond length at the GB makes it difficult to clarify the GB EELS intensity change with specific defect modes or phonon branches, since changes in each bond length would result in collective changes of the whole dispersion diagram by changing the energy of certain vibrational modes and also introducing new characteristic vibrational modes (as described in Figure S2 and Supplementary Note 1). This change can be understood by the sensitivity of force constant to the chemical bond length. Basically, the bonding lengths at general GBs are totally different from that of bulk, which would compose of a wide distribution of bond length. Therefore, it is expected that general GBs in Al_2O_3, even with different geometry configurations, would exhibit similar defect phonon DOS. Our present findings differ from those GB phonon structures in $SrTiO_3$ and Si reported so far.[27,28] For example, Hoglund et al.'s study of the $SrTiO_3$ GB provided evidence in correlating the coordination, chemistry, bonding, and electronic states with vibrational modes,[27] while our study found that for Al_2O_3 the change in bond length is the dominant one. Furthermore, our findings in Al_2O_3 also differ from that in Si defects, where it is reported that bond angle dominates GB vibrational modes.[28] Therefore, it seems that the dominant factor to determine the local defect phonon can be very different in different materials. All of these results highlight the complexity of understanding general rules for phonon structures at local defects in a variety of materials.

On the other hand, the existence of localized unique phonons at GBs is expected to substantially affect thermal transport in polycrystalline Al_2O_3 ceramics. Specifically, the vibrational EELS spectra of GBs show lower intensity at an energy range of 50−80 meV, indicating a smaller phonon population in this energy range. Based on the diffusive mismatch model (DDM) mode, the reduction of phonon DOS would to a certain degree impede the transportation of the lattice wave at GB and result in a higher local thermal resistance for these frequencies;[43] therefore, the increase of phonon population at energy range of <50 meV and >80 meV would not make a significant change. Furthermore, most optical phonon branches of Al_2O_3 reside in the energy range of 50−80 meV,[44] indicating the GB thermal resistance mainly originated from the scattering of optical phonons.[41,45−47] Additionally, since the optical phonons are closely related with the electron−phonon coupling and optical propagation such as phonon polaritons, the significant change of optical phonons at the GB is also expected to play an important role in the local electrical and optical properties, which will stimulate further studies in the future.

In summary, we directly measured the localized phonon modes of the Al_2O_3 GBs, and we found a reduced vibration at the energy range of 50−80 meV and enhanced vibration at <50 meV and >80 meV. The overall projected DOS of local phonons is not sensitive to the GB geometry. Such local phonon structures are mainly dominated by the wide distribution of bond lengths in GBs. Our direct conclusion would be of great importance in the grain boundary engineering of Al_2O_3 in regulating its thermal, electrical, and optical properties, in applications such as being the heat transfer and storage medium in solar particle recerivers,[48] the high-quality filler of thermal conductive and electrical insulated composites,[49] and also optical windows for lasers, spectrometers, armor parts, and IR-domes for infrared missile guidance system.[50] Moreover, our self-consistent scheme provides new insights in investigating the phonon structure of the general polycrystalline materials and would be of great importance in addressing the structure-phonon-property relationships among a wider category of materials.

SAMPLE PREPARATION

Bicrystal specimens were used to obtain a well-defined single GB. In this way, well-controlled experiments can be performed, and the effect of other defects in the polycrystalline materials can be eliminated.[37] The Al_2O_3 bicrystals were fabricated by the thermal diffusion bonding of two single crystals (Shinkosha Co., Ltd.) at 1500 °C under 0.1 MPa for 10 h in air.[38,51,52] TEM samples were fabricated by mechanical grinding followed by ion milling using a Precision Ion Polishing System (PIPS, model 691, Gatan) to further thin it to ∼50 nm.

In this study, several types of GBs, such as $\sum$7a, $\sum$19a, and $\sum$31 GBs, were systematically fabricated to investigate GB character dependency.

VIBRATIONAL EELS AND IMAGING EXPERIMENTS

The vibrational spectra were measured by a Nion microscope U-HERMES200. The EELS data sets are acquired at 60 kV with a convergence semiangle of 20 mrad and a collection semiangle of 25 mrad to ensure sufficient space and energy resolutions. As Al_2O_3 is sensitive to electron beam irradiation,[53] the acquisition time for each pixel was set to 4 s, and a 40 pixel ×10 pixel 2D EELS mapping data set was acquired in an area of 8 nm × 2 nm containing a GB at the center. An off-axis condition was used to mitigate the strong polariton signal of Al_2O_3 from Γ point,[40,54] although such conditions drastically reduce the acquisition signals. In our case, the electron beam was shifted ∼50 mrad away from the center beam axis, along the symmetric direction of the Kikuchi pattern of the bicrystal system to reduce the elastically transmitted electrons from being collected by the EELS aperture while ensuring the signals of both grains were collected equally to avoid the differences introduced by the relative positions of the EELS aperture and diffraction pattern. The energy resolution is ∼10 meV, and the spatial resolution is ∼1 nm. iDPC and part of the HAADF images were recorded at 300 kV, using an aberration-corrected FEI Titan Themis G2 with spatial resolution up to 60 pm. The convergence semiangle for imaging is 30 mrad, and the collection semiangle snap is 4 to 21 mrad for the iDPC imaging and 39 to 200 mrad for the HAADF.

EELS DATA PROCESSING

All acquired spectra were processed by custom-written Matlab code. The spectra were first aligned by zero-loss peaks to correct possible beam energy drift. A block-matching and 3D filtering (BM3D) algorithm was applied to remove Gaussian noise.[55,56] The tail of the zero-loss peak is fitted with a Pearson function with two fitting windows and then subtracted in order to obtain the vibrational signal.[41,57] The fitting windows are selected to make the background-subtracted spectra at the bulk

https://doi.org/10.1021/acs.nanolett.3c04149
Nano Lett. XXXX, XXX, XXX−XXX

area best fit the simulated EELS spectrum of bulk Al_2O_3. The statistical factors of the background-subtracted spectra, which were resulted from the different scattering probability of phonons with different frequency, were further corrected to make the spectra more comparable to the real phonon DOS.[58]

DENSITY FUNCTIONAL PERTURBATION THEORY (DFPT) SIMULATION

The DFPT simulations were conducted using the Quantum Espresso[59,60] with the PBE Exchange-Correlation functional and Ultrasoft pseudopotential[61] for O and norm-conserving pseudopotential[62] for Al. The cutoff of the wave functions is 25 Ry (Ry) and 225 Ry of the charge density and potential.

The phonon dispersion and PDOS was calculated by interpolating the dynamical matrix on a 3 × 3 × 3 q-mesh. The cross-section of the scattering electrons for an infinite bulk crystal can be interpreted as[20,63,64]

$$\frac{d^2\sigma}{d\omega d\Omega} \propto \sum_{mode\lambda} |F_\lambda(\mathbf{q})|^2 \left[\frac{n+1}{\omega_\lambda(\mathbf{q})} \delta(\omega - \omega_\lambda(\mathbf{q})) + \frac{n}{\omega_\lambda(\mathbf{q})} \delta(\omega - \omega_\lambda(\mathbf{q})) \right]$$

where $\omega_\lambda(\mathbf{q})$ and n are the frequency and occupancy number of the λ^{th} phonon mode with wavevector $\mathbf{q}$. The two terms in the square brackets correspond to phonon emission and absorption processes, respectively. The coupling factor

$$F_\lambda(\mathbf{q}) \propto \frac{1}{q^2} \sum_{atomk} \frac{1}{\sqrt{M_k}} e^{-i\mathbf{q}\cdot\mathbf{r}_k} e^{-W_k(\mathbf{q})} + Z_k(\mathbf{q})[\mathbf{e}_\lambda(k, \mathbf{q})\cdot\mathbf{q}]$$

is determined by the mass M_k, real-space position $\mathbf{r}_k$, effective charge $Z_k(\mathbf{q})$, Debye–Waller factor[65] $\exp(-2W_k(\mathbf{q}))$, and phonon eigenvector $e_\lambda(k, \mathbf{q})$ of the k^{th} atom in a unit cell. The effective charge $Z_k(\mathbf{q})$ was calculated following the literature with atomic form factors constructed from parameters in the literature.[59]

ASSOCIATED CONTENT

Supporting Information

The Supporting Information is available free of charge at https://pubs.acs.org/doi/10.1021/acs.nanolett.3c04149.

Bond length distribution of GBs with different misorientations (Supplementary Figure S1), phonon dispersion and eigenvector of cells with different bond lengths (Supplementary Figure S2), and extended discussions in how changes in bond length modify the phonon structures (Supplementary Note 1) (PDF)

AUTHOR INFORMATION

Corresponding Authors

Bin Feng − *Institute of Engineering Innovation, The University of Tokyo, Tokyo 113-8656, Japan; PRESTO, Japan Science and Technology Agency, Kawaguchi 332-0012, Japan;* orcid.org/0000-0002-4306-2979; Email: feng@sigma.t.u-tokyo.ac.jp

Peng Gao − *Electron Microscopy Laboratory, School of Physics, International Center for Quantum Materials, and Interdisciplinary Institute of Light-Element Quantum Materials and Research Center for Light-Element Advanced Materials, Peking University, Beijing 100871, China;* orcid.org/0000-0003-0860-5525; Email: pgao@pku.edu.cn

Yuichi Ikuhara − *Institute of Engineering Innovation, The University of Tokyo, Tokyo 113-8656, Japan; Nanostructures Research Laboratory, Japan Fine Ceramics Center, Nagoya 456-8587, Japan;* orcid.org/0000-0003-3886-005X; Email: ikuhara@sigma.t.u-tokyo.ac.jp

Authors

Jingyuan Yan − *Institute of Engineering Innovation, The University of Tokyo, Tokyo 113-8656, Japan; Electron Microscopy Laboratory, School of Physics, Peking University, Beijing 100871, China;* orcid.org/0009-0008-7154-1919

Ruochen Shi − *Electron Microscopy Laboratory, School of Physics and International Center for Quantum Materials, Peking University, Beijing 100871, China*

Jiake Wei − *Institute of Engineering Innovation, The University of Tokyo, Tokyo 113-8656, Japan; State Key Laboratory of Catalysis, Dalian Institute of Chemical Physics, Chinese Academy of Sciences, Dalian 116023, China;* orcid.org/0000-0001-7450-7005

Yuehui Li − *Electron Microscopy Laboratory, School of Physics and International Center for Quantum Materials, Peking University, Beijing 100871, China*

Ruishi Qi − *Electron Microscopy Laboratory, School of Physics and International Center for Quantum Materials, Peking University, Beijing 100871, China; Department of Physics, University of California at Berkeley, Berkeley 94720 California, United States*

Mei Wu − *Electron Microscopy Laboratory, School of Physics and International Center for Quantum Materials, Peking University, Beijing 100871, China*

Xiaomei Li − *Electron Microscopy Laboratory, School of Physics, Peking University, Beijing 100871, China; School of Integrated Circuits, East China Normal University, Shanghai 200241, China*

Naoya Shibata − *Institute of Engineering Innovation, The University of Tokyo, Tokyo 113-8656, Japan; Nanostructures Research Laboratory, Japan Fine Ceramics Center, Nagoya 456-8587, Japan;* orcid.org/0000-0003-3548-5952

Complete contact information is available at: https://pubs.acs.org/10.1021/acs.nanolett.3c04149

Notes

The authors declare no competing financial interest.

ACKNOWLEDGMENTS

This work was supported by a Grants-in-Aid for Scientific Research (Grant No. JP22H04960), a Grants-in-Aid for Scientific Research on Innovative Areas (Grant No. JP19H05788), and a Grants-in-Aid for Early-Career Scientists (JP22K14463) by Japan Society for the Promotion of Science (JSPS). B.F. acknowledges support by JST-PRESTO (Grant JPMJPR23JB), Japan. P.G. acknowledges the support from the National Natural Science Foundation of China (52125307) and New Cornerstone Science Foundation through the XPLORER PRIZE. We acknowledge Electron Microscopy Laboratory of Peking University for the use of electron microscopes. And we also thank Prof. Michael Finnis from Imperial College London and Toshihiro Futazuka from The University of Tokyo for sharing their theoretically obtained atomic structures of Al_2O_3 grain boundaries.

REFERENCES

(1) Krumhansl, J. Lattice vibrations in solids. *J. Appl. Phys.* **1962**, *33* (1), 307−319.
(2) Anees, P.; Valsakumar, M.; Panigrahi, B. Effect of strong phonon−phonon coupling on the temperature dependent structural stability and frequency shift of 2D hexagonal boron nitride. *Phys. Chem. Chem. Phys.* **2016**, *18* (4), 2672−2681.
(3) Khandy, S. A.; Chai, J.-D. Origin of pseudo gap and thermoelectric signatures of semimetallic Ru2TaGa: Structural stability from phonon dynamics, mechanical, and thermodynamic predictions. *J. Phys. Chem. Solids* **2021**, *154*, 110098.
(4) Su, L.; Wang, D.; Wang, S.; Qin, B.; Wang, Y.; Qin, Y.; Jin, Y.; Chang, C.; Zhao, L.-D. High thermoelectric performance realized through manipulating layered phonon-electron decoupling. *Science* **2022**, *375* (6587), 1385−1389.
(5) Liu, H.; Yuan, X.; Lu, P.; Shi, X.; Xu, F.; He, Y.; Tang, Y.; Bai, S.; Zhang, W.; Chen, L.; et al. Ultrahigh thermoelectric performance by electron and phonon critical scattering in Cu2Se1-xIx. *Adv. Mater.* **2013**, *25* (45), 6607−6612.
(6) Masri, P. Surface and interface phonons and related topics. *Surf. Sci. Rep.* **1988**, *9* (7−8), 293−369.
(7) Peng, F.; Chen, N.-x. Amplification of the interface-phonon population under an intense laser field. *Phys. Rev. B* **1992**, *46* (12), 7627−7631.
(8) Gordiz, K.; Henry, A. Phonon transport at interfaces: Determining the correct modes of vibration. *J. Appl. Phys.* **2016**, *119* (1), No. 015101.
(9) Li, M.; Ding, Z.; Meng, Q.; Zhou, J.; Zhu, Y.; Liu, H.; Dresselhaus, M. S.; Chen, G. Nonperturbative quantum nature of the dislocation−phonon interaction. *Nano Lett.* **2017**, *17* (3), 1587−1594.
(10) Kim, H.-S.; Kang, S. D.; Tang, Y.; Hanus, R.; Snyder, G. J. Dislocation strain as the mechanism of phonon scattering at grain boundaries. *Materials Horizons* **2016**, *3* (3), 234−240.
(11) Schelling, P.; Phillpot, S.; Keblinski, P. Kapitza conductance and phonon scattering at grain boundaries by simulation. *J. Appl. Phys.* **2004**, *95* (11), 6082−6091.
(12) Smith, D. S.; Grandjean, S.; Absi, J.; Kadiebu, S.; Fayette, S. Grain-boundary thermal resistance in polycrystalline oxides: alumina, tin oxide, and magnesia. *High Temperatures-High Pressures* **2003**, *35* (1), 93−100.
(13) McCreery, R. L. *Raman spectroscopy for chemical analysis;* John Wiley & Sons, 2005.
(14) Stuart, B. H. *Infrared spectroscopy: fundamentals and applications;* John Wiley & Sons, 2004 DOI: 10.1002/0470011149.
(15) Chan, K.; Kazarian, S. New opportunities in micro-and macro-attenuated total reflection infrared spectroscopic imaging: spatial resolution and sampling versatility. *Applied spectroscopy* **2003**, *57* (4), 381−389.
(16) Burkel, E. Phonon spectroscopy by inelastic x-ray scattering. *Rep. Prog. Phys.* **2000**, *63* (2), 171.
(17) Mitchell, P. C. H. *Vibrational spectroscopy with neutrons: with applications in chemistry, biology, materials science and catalysis;* World Scientific, 2005; Vol. 3 DOI: 10.1142/5628.
(18) Krivanek, O. L.; Lovejoy, T. C.; Dellby, N.; Aoki, T.; Carpenter, R.; Rez, P.; Soignard, E.; Zhu, J.; Batson, P. E.; Lagos, M. J.; et al. Vibrational spectroscopy in the electron microscope. *Nature* **2014**, *514* (7521), 209−212.
(19) Egerton, R. Vibrational-loss EELS and the avoidance of radiation damage. *Ultramicroscopy* **2015**, *159*, 95−100.
(20) Lagos, M. J.; Trügler, A.; Hohenester, U.; Batson, P. E. Mapping vibrational surface and bulk modes in a single nanocube. *Nature* **2017**, *543* (7646), 529−532.
(21) Hachtel, J. A.; Huang, J.; Popovs, I.; Jansone-Popova, S.; Keum, J. K.; Jakowski, J.; Lovejoy, T. C.; Dellby, N.; Krivanek, O. L.; Idrobo, J. C. Identification of site-specific isotopic labels by vibrational spectroscopy in the electron microscope. *Science* **2019**, *363* (6426), 525−528.
(22) Zeiger, P. M.; Rusz, J. Efficient and versatile model for vibrational STEM-EELS. *Phys. Rev. Lett.* **2020**, *124* (2), No. 025501.
(23) Rez, P.; Singh, A. Lattice resolution of vibrational modes in the electron microscope. *Ultramicroscopy* **2021**, *220*, 113162.
(24) Colliex, C. From early to present and future achievements of EELS in the TEM. *European Physical Journal Applied Physics* **2022**, *97*, 38.
(25) Xu, M.; Bao, D.-L.; Li, A.; Gao, M.; Meng, D.; Li, A.; Du, S.; Su, G.; Pennycook, S. J.; Pantelides, S. T.; et al. Single-atom vibrational spectroscopy with chemical-bonding sensitivity. *Nat. Mater.* **2023**, *22* (5), 612−618.
(26) Ko, W.; Gai, Z.; Puretzky, A. A.; Liang, L.; Berlijn, T.; Hachtel, J. A.; Xiao, K.; Ganesh, P.; Yoon, M.; Li, A. P. Understanding heterogeneities in quantum materials. *Adv. Mater.* **2023**, *35* (27), 2106909.
(27) Hoglund, E. R.; Bao, D. L.; O'Hara, A.; Pfeifer, T. W.; Hoque, M. S. B.; Makarem, S.; Howe, J. M.; Pantelides, S. T.; Hopkins, P. E.; Hachtel, J. A. Direct Visualization of Localized Vibrations At Complex Grain Boundaries. *Adv. Mater.* **2023**, *35* (13), 2208920.
(28) Haas, B.; Boland, T. M.; Elsässer, C.; Singh, A. K.; March, K.; Barthel, J.; Koch, C. T.; Rez, P. Atomic-Resolution Mapping of Localized Phonon Modes at Grain Boundaries. *Nano Lett.* **2023**, *23* (13), 5975−5980.
(29) Hoglund, E. R.; Bao, D.-L.; O'Hara, A.; Makarem, S.; Piontkowski, Z. T.; Matson, J. R.; Yadav, A. K.; Haislmaier, R. C.; Engel-Herbert, R.; Ihlefeld, J. F.; et al. Emergent interface vibrational structure of oxide superlattices. *Nature* **2022**, *601* (7894), 556−561.
(30) Gadre, C. A.; Yan, X.; Song, Q.; Li, J.; Gu, L.; Huyan, H.; Aoki, T.; Lee, S.-W.; Chen, G.; Wu, R.; et al. Nanoscale imaging of phonon dynamics by electron microscopy. *Nature* **2022**, *606* (7913), 292−297.
(31) Hossain, M. S.; Nakane, K. Development of a high-performance heat dissipation sheet with three-dimensional alumina fibrous structure fabricated by freeze-drying. *Results in Materials* **2022**, *13*, 100241.
(32) Peterson, R. E.; Ramsey, J. Thin film coatings in solar− thermal power systems. *J. Vac. Sci. Technol.* **1975**, *12* (1), 174−181.
(33) Andrews, D. L. *Photonics, volume 3: Photonics technology and instrumentation;* John Wiley & Sons, 2015; Vol. 3.
(34) Giustino, F. Electron-phonon interactions from first principles. *Rev. Mod. Phys.* **2017**, *89* (1), No. 015003.
(35) Lazić, I.; Bosch, E. G. Analytical review of direct STEM imaging techniques for thin samples. *Advances in Imaging and Electron Physics* **2017**, *199*, 75−184.
(36) Yang, C.; Feng, B.; Wei, J.; Tochigi, E.; Ishihara, S.; Shibata, N.; Ikuhara, Y. Atomic and electronic band structures of Ti-doped Al2O3 grain boundaries. *Acta Mater.* **2020**, *201*, 488−493.
(37) Wei, J.; Feng, B.; Ishikawa, R.; Yokoi, T.; Matsunaga, K.; Shibata, N.; Ikuhara, Y. Direct imaging of atomistic grain boundary migration. *Nat. Mater.* **2021**, *20* (7), 951−955.
(38) Nishimura, H.; Matsunaga, K.; Saito, T.; Yamamoto, T.; Ikuhara, Y. Atomic structures and energies of Σ7 symmetrical tilt grain boundaries in alumina bicrystals. *J. Am. Ceram. Soc.* **2003**, *86* (4), 574−80.
(39) Guhl, H.; Lee, H.-S.; Tangney, P.; Foulkes, W.; Heuer, A. H.; Nakagawa, T.; Ikuhara, Y.; Finnis, M. W. Structural and electronic properties of Σ7 grain boundaries in α-Al2O3. *Acta Mater.* **2015**, *99*, 16−28.
(40) Hage, F.; Radtke, G.; Kepaptsoglou, D.; Lazzeri, M.; Ramasse, Q. Single-atom vibrational spectroscopy in the scanning transmission electron microscope. *Science* **2020**, *367* (6482), 1124−1127.
(41) Qi, R.; Shi, R.; Li, Y.; Sun, Y.; Wu, M.; Li, N.; Du, J.; Liu, K.; Chen, C.; Chen, J.; et al. Measuring phonon dispersion at an interface. *Nature* **2021**, *599* (7885), 399−403.
(42) Yan, X.; Liu, C.; Gadre, C. A.; Gu, L.; Aoki, T.; Lovejoy, T. C.; Dellby, N.; Krivanek, O. L.; Schlom, D. G.; Wu, R.; et al. Single-defect phonons imaged by electron microscopy. *Nature* **2021**, *589* (7840), 65−69.

https://doi.org/10.1021/acs.nanolett.3c04149
Nano Lett. XXXX, XXX, XXX−XXX

(43) Zheng, Z.; Chen, X.; Deng, B.; Chernatynskiy, A.; Yang, S.; Xiong, L.; Chen, Y. Phonon thermal transport through tilt grain boundaries in strontium titanate. *J. Appl. Phys.* **2014**, *116* (7), No. 073706.
(44) Jain, A.; Ong, S. P.; Hautier, G.; Chen, W.; Richards, W. D.; Dacek, S.; Cholia, S.; Gunter, D.; Skinner, D.; Ceder, G.; et al. Commentary: The Materials Project: A materials genome approach to accelerating materials innovation. *APL materials* **2013**, *1* (1), No. 011002.
(45) Ward, A.; Broido, D. A. Intrinsic phonon relaxation times from first-principles studies of the thermal conductivities of Si and Ge. *Phys. Rev. B* **2010**, *81* (8), No. 085205.
(46) Ward, A.; Broido, D. A.; Stewart, D. A.; Deinzer, G. Ab initio theory of the lattice thermal conductivity in diamond. *Phys. Rev. B* **2009**, *80* (12), 125203.
(47) Broido, D. A.; Malorny, M.; Birner, G.; Mingo, N.; Stewart, D. A. Intrinsic lattice thermal conductivity of semiconductors from first principles. *Appl. Phys. Lett.* **2007**, *91*, 231922.
(48) Chen, J.; Wheeler, V. M.; Liu, B.; Kumar, A.; Coventry, J.; Lipiński, W. Optical characterisation of alumina−mullite materials for solar particle receiver applications. *Sol. Energy Mater. Sol. Cells* **2021**, *230*, 111170.
(49) Ouyang, Y.; Bai, L.; Tian, H.; Li, X.; Yuan, F. Recent progress of thermal conductive ploymer composites: Al2O3 fillers, properties and applications. *Composites Part A: Applied Science and Manufacturing* **2022**, *152*, 106685.
(50) Cheng, J.; Agrawal, D.; Zhang, Y.; Roy, R. Microwave sintering of transparent alumina. *Mater. Lett.* **2002**, *56* (4), 587−592.
(51) Ishihara, S.; Tochigi, E.; Ishikawa, R.; Shibata, N.; Ikuhara, Y. Coexistence of two different atomic structures in the Σ13 pyramidal twin boundary in α-Al2O3. *Philosophical Magazine Letters* **2019**, *99* (12), 435−443.
(52) Matsunaga, K.; Nishimura, H.; Saito, T.; Yamamoto, T.; Ikuhara, Y. High-resolution transmission electron microscopy and computational analyses of atomic structures of [0001] symmetric tilt grain boundaries of Al2O3 with equivalent grain-boundary planes. *Philos. Mag.* **2003**, *83* (36), 4071−4082.
(53) Bonevich, J. E.; Marks, L. D. Electron radiation damage of α-alumina. *Ultramicroscopy* **1991**, *35* (2), 161−166.
(54) Hage, F.; Kepaptsoglou, D.; Ramasse, Q.; Allen, L. Phonon spectroscopy at atomic resolution. *Physical review letters* **2019**, *122* (1), No. 016103.
(55) Zhou, J.; Yang, Y.; Yang, Y.; Kim, D. S.; Yuan, A.; Tian, X.; Ophus, C.; Sun, F.; Schmid, A. K.; Nathanson, M.; et al. Observing crystal nucleation in four dimensions using atomic electron tomography. *Nature* **2019**, *570* (7762), 500−503.
(56) Dabov, K.; Foi, A.; Katkovnik, V.; Egiazarian, K. Image denoising by sparse 3-D transform-domain collaborative filtering. *IEEE Transactions on image processing* **2007**, *16* (8), 2080−2095.
(57) Li, N.; Shi, R.; Li, Y.; Qi, R.; Liu, F.; Zhang, X.; Liu, Z.; Li, Y.; Guo, X.; Liu, K.; Jiang, Y.; Li, X.-Z.; Chen, J.; Liu, L.; Wang, E.-G.; Gao, P. Phonon transition across an isotopic interface. *Nat. Commun.* **2023**, *14* (1), 2382.
(58) Batson, P.; Lagos, M. Interpretation of meV resolution phonon EELS data. *Microscopy and Microanalysis* **2018**, *24* (S1), 412−413.
(59) Giannozzi, P.; Baroni, S.; Bonini, N.; Calandra, M.; Car, R.; Cavazzoni, C.; Ceresoli, D.; Chiarotti, G. L.; Cococcioni, M.; Dabo, I.; et al. QUANTUM ESPRESSO: a modular and open-source software project for quantum simulations of materials. *J. Phys.: Condens. Matter* **2009**, *21* (39), 395502.
(60) Giannozzi, P.; Andreussi, O.; Brumme, T.; Bunau, O.; Buongiorno Nardelli, M.; Calandra, M.; Car, R.; Cavazzoni, C.; Ceresoli, D.; Cococcioni, M. Advanced capabilities for materials modelling with Quantum ESPRESSO. *J. Phys.: Condens. Matter* **2017**, *29* (46), 465901.
(61) Kresse, G.; Joubert, D. From ultrasoft pseudopotentials to the projector augmented-wave method. *Physical review b* **1999**, *59* (3), 1758.
(62) Hamann, D.; Schlüter, M.; Chiang, C. Norm-conserving pseudopotentials. *Phys. Rev. Lett.* **1979**, *43* (20), 1494.
(63) Senga, R.; Suenaga, K.; Barone, P.; Morishita, S.; Mauri, F.; Pichler, T. Position and momentum mapping of vibrations in graphene nanostructures. *Nature* **2019**, *573* (7773), 247−250.
(64) Nicholls, R.; Hage, F.; McCulloch, D.; Ramasse, Q.; Refson, K.; Yates, J. Theory of momentum-resolved phonon spectroscopy in the electron microscope. *Phys. Rev. B* **2019**, *99* (9), No. 094105.
(65) Vila, F. D.; Rehr, J.; Rossner, H.; Krappe, H. Theoretical x-ray absorption Debye-Waller factors. *Phys. Rev. B* **2007**, *76* (1), No. 014301.

https://doi.org/10.1021/acs.nanolett.3c04149
Nano Lett. XXXX, XXX, XXX−XXX